

Time-varying parametric subharmonic instability from repeat CTD surveys in the northwestern Pacific Ocean

Bo Qiu,¹ Shuiming Chen,¹ and Glenn S. Carter¹

Received 10 January 2012; revised 27 July 2012; accepted 1 August 2012; published 12 September 2012.

[1] Time-varying diapycnal diffusivity signals are estimated using the fine-scale parameterization method from high-resolution CTD data along three repeat sections in the northwestern Pacific Ocean. Indicative of the parametric subharmonic instability (PSI), locally-elevated diapycnal mixing is detected along *all* three sections within the 25°–29°N band where bottom topography is relatively featureless. Due to their proximity to the semidiurnal internal tide generation sites, the two sections along ~137°E have a time-mean diffusivity value $2.5 \times 10^{-5} \text{ m}^2 \text{ s}^{-1}$ in the 300–2,000 m upper ocean. In contrast, it is $1.2 \times 10^{-5} \text{ m}^2 \text{ s}^{-1}$ along the 165°E section. The time-varying diffusivity along both sections is dominated by signals whose vertical structure resembles the local first dynamic normal mode profile. At the 137°E site of 25°–29°N, the local spring-neap modulated semidiurnal tidal current is found to lead the CTD-derived diffusivity time series by 6 days and can alter the diffusivity level by $0.24 \times 10^{-5} \text{ m}^2 \text{ s}^{-1}$. Similarly, the concurrent surface wind work is found to modify the diffusivity level by $0.35 \times 10^{-5} \text{ m}^2 \text{ s}^{-1}$. The combined spring-neap tide and wind work forcing explains 47% of the observed, time-varying diffusivity signals.

Citation: Qiu, B., S. Chen, and G. S. Carter (2012), Time-varying parametric subharmonic instability from repeat CTD surveys in the northwestern Pacific Ocean, *J. Geophys. Res.*, 117, C09012, doi:10.1029/2012JC007882.

1. Introduction

[2] Parametric subharmonic instability (PSI) signifies the nonlinear triad interaction in which wave energy is converted from high-frequency/low-vertical-wave number modes to low-frequency/high-wave number modes. Although PSI's relevance in transferring energy from semidiurnal internal tides to near-inertial internal waves near the critical latitude of 28.9° was theorized in the 1970s [e.g., *McComas and Bretherton*, 1977; *Muller et al.*, 1986], it is not until the last decade has a renewed interest in PSI re-emerged. This renewed interest is stimulated by newly available observational and numerical modeling studies that demonstrate PSI works as an energy source for the interior ocean mixing and an energy sink for the semidiurnal internal tides.

[3] In the North Pacific Ocean, observational evidence for enhanced diapycnal diffusivity in the latitudinal band just equatorward of 28.9°N was provided by *Nagasawa et al.* [2002] and *Hibiya and Nagasawa* [2004] using expandable current profiler measurements, by *Kunze et al.* [2006] with the use of WOCE conductivity-temperature-depth/lowered acoustic Doppler current profiler (CTD/LADCP) data, and by *Tian et al.* [2006] based on internal tide energy flux convergence inferred from satellite altimeter data. Energy

transfers from the M_2 internal tides to the diurnal internal waves were also detected in the Hawaii Ocean Mixing Experiment (HOME) and near the critical latitude north of the Hawaiian Ridge in the recent Internal Waves Across the Pacific (IWAP) experiment dedicated to unravel the PSI-related processes [*Carter and Gregg*, 2006; *Rainville and Pinkel*, 2006; *Alford et al.*, 2007; *Zhao et al.*, 2010].

[4] Numerically, the importance of PSI in causing a significant internal tidal energy loss near the critical latitude of 28.9° was first demonstrated by *MacKinnon and Winters* [2005] using an idealized model simulation. Their work has recently been extended by *Hazewinkel and Winters* [2011] with simulations under a more realistic oceanic setting. Compared to the *MacKinnon and Winters's* [2005] result, a more moderate (of ~15%), PSI-induced reduction in internal tide energy was found by *Hazewinkel and Winters* [2011]. Using a global baroclinic tidal model with realistic geometry, *Simmons* [2008] investigated the internal tide generation and found an energy transfer to the $M_2/2$ subharmonic modes that is concentrated along the critical latitudes in *all* world oceans.

[5] While evidence for PSI-induced turbulent mixing is building, our knowledge about its time-varying signals is still lacking. With the improvement in parameterization methods to infer the diapycnal diffusivity [see *Kunze et al.*, 2006, and references therein], high-resolution CTD surveys along repeat hydrographic sections provide a useful means to explore the time-varying mixing signals of a PSI origin. In the northwestern Pacific Ocean, three such repeat CTD survey sections have been maintained by Japan Meteorological Agency (JMA) over the past 15 years. The objective

¹Department of Oceanography, University of Hawai'i at Mānoa, Honolulu, Hawaii, USA.

Corresponding author: B. Qiu, Department of Oceanography, University of Hawai'i at Mānoa, Honolulu, HI 96822, USA. (bo@soest.hawaii.edu)

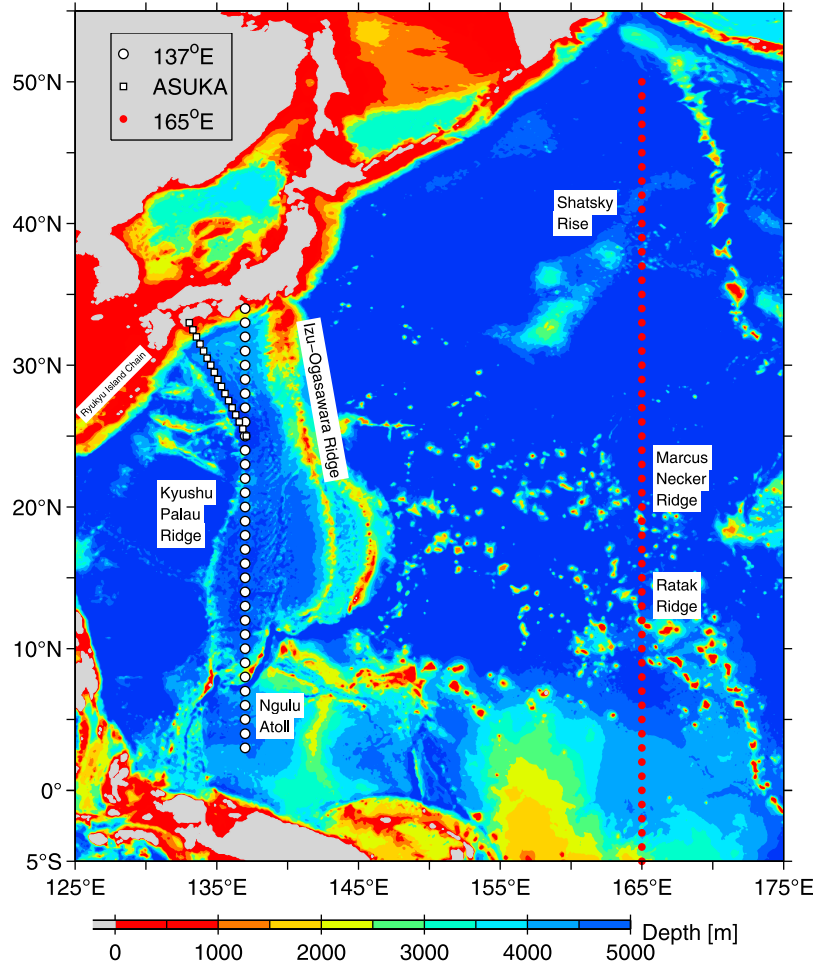


Figure 1. Locations of nominal CTD stations along the JMA’s 137°E, 165°E, and ASUKA repeat hydrographic sections. Colored map shows the bathymetry based on *Smith and Sandwell* [1997].

of the present study is to examine the diapycnal diffusivity signals based on these long-term repeat CTD surveys. In particular, we will focus on the temporal changes in diapycnal diffusivity in the latitudinal band of 25°–29°N and attempt to quantify their connections to the energy input by spring-neap modulated semidiurnal tides and by synoptic-scale surface wind forcing on near-inertial motions.

2. Data and Methods

[6] Repeat CTD surveys have been carried out by JMA in the northwestern Pacific Ocean along the 137°E meridian from 34°N to 3°N, the 165°E meridian from 50°N to 5°S, and an oblique line from Cape Ashizuri (at 33°N and 133°E) to 25°N and 137°E (Figure 1). This last oblique line is commonly known as the ASUKA line and coincides with a ground track of the TOPEX/Poseidon satellite [e.g., *Imawaki et al.*, 2001]. All JMA CTD surveys have a 1- or 2-dbar vertical resolution and fully cover the 2,000 m upper ocean. For the present study, we use 53 surveys along 137°E that are available seasonally since 1997, 21 surveys along 165°E available either annually or semiannually since 1997, and 38 surveys along the ASUKA line available seasonally since 2001. Latitudinally, the CTD casts have a nominal 1° resolution along

137°E and 165°E, and a nominal 0.5° resolution along the ASUKA line.

[7] To infer the diapycnal diffusivity K from the individual CTD casts, we adopt the fine-scale parameterization method proposed by *Kunze et al.* [2006]

$$K = K_0 \frac{\langle \xi_z^2 \rangle}{GM \langle \xi_z^2 \rangle} h_2(R_\omega) j\left(\frac{f}{N}\right), \quad (1)$$

where $K_0 = 0.5 \times 10^{-5} \text{ m}^2 \text{ s}^{-1}$, $GM \langle \xi_z^2 \rangle$ is strain variance from the Garrett-Munk model spectrum [e.g., *Gregg and Kunze*, 1991], f is the Coriolis parameter, and N is the buoyancy frequency. In equation (1),

$$h_2(R_\omega) = \frac{1}{6\sqrt{2}} \frac{R_\omega (R_\omega + 1)}{\sqrt{R_\omega - 1}},$$

$$j(f/N) = \frac{f \cosh^{-1}(N/f)}{f_{30} \cosh^{-1}(N_0/f_{30})},$$

where $f_{30} = f_{30^\circ}$, $N_0 = 5.2 \times 10^{-3} \text{ rad s}^{-1}$, and R_ω represents the shear/strain variance ratio and is set at 7 following *Kunze et al.* [2006]. The strain variance $\langle \xi_z^2 \rangle$ in (1) is evaluated in the vertically overlapping segments of 256 m. Within each

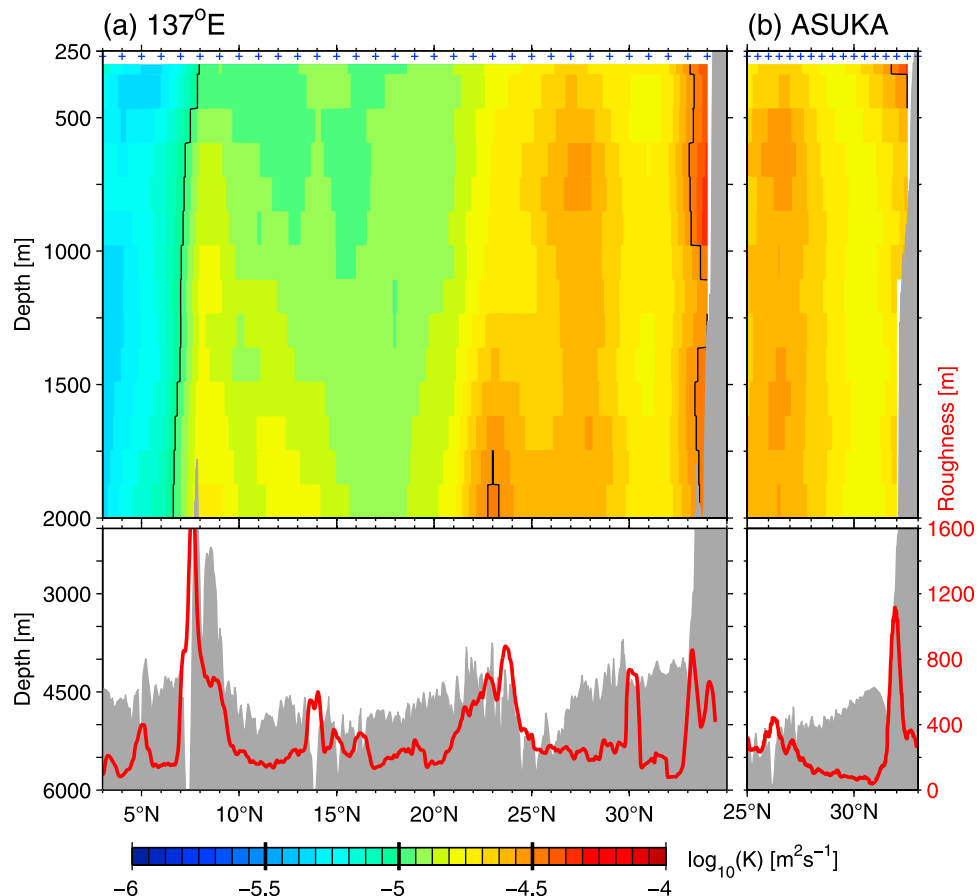


Figure 2. (a, top) Latitude-depth section of the time-mean diapycnal diffusivity K inferred from 57 repeat CTD surveys along the 137°E meridian. Grey shade denotes the bathymetry of *Smith and Sandwell* [1997]. (a, bottom) The red curve shows the roughness of bathymetry defined as the RMS bathymetric height variance in a $32\text{ km} \times 32\text{ km}$ square. (b) Same as Figure 2a except for along the ASUKA line.

segment, we first obtain $\xi_z = \left(N^2(z) - \overline{N^2}\right)/\overline{N^2}$, where $\overline{N^2}$ denotes the squared buoyancy frequency low-pass filtered with a Gaussian decay scale of 50 m, and calculate its spectrum $\phi(k)$, where k is the vertical wave number. The strain variance is then derived by integrating $\phi(k)$ from a minimum wave number $k_{\min} = 2\pi/150\text{ m}$ to a maximum wave number k_{\max} such that

$$\langle \xi_z^2 \rangle = \int_{k_{\min}}^{k_{\max}} \phi(k) dk = 0.1. \quad (2)$$

As rationalized in *Kunze et al.* [2006], the GM model strain variance $_{GM}\langle \xi_z^2 \rangle$ used for normalization in (1) is computed over this same wave number band. For $j(f/N)$ in equation (1), N is given by the square root of $\overline{N^2}$. To avoid contamination by surface layer processes, the surface 300 m layer is excluded from the K estimation.

3. Time-Mean Diapycnal Eddy Diffusivity

[8] Figure 2a shows the latitude-depth section of the inferred diapycnal diffusivity averaged over the 53 CTD surveys along 137°E . Consistent with the existing studies by *Gregg et al.* [2003] and *Kunze et al.* [2006] among others,

the inferred diapycnal diffusivity is very weak near the equator ($\sim 0.5 \times 10^{-6}\text{ m}^2\text{ s}^{-1}$), and has a broad-scale tendency to increase with increasing latitude. Both of these two characters are related to the factor $j(f/N)$ used in the fine-scale parameterization (1). Superimposed on this broad-scale increasing trend, localized high K values are detected in the bands of $8^\circ\text{--}10^\circ\text{N}$, $22^\circ\text{--}24^\circ\text{N}$, $25^\circ\text{--}29^\circ\text{N}$, and $32^\circ\text{--}34^\circ\text{N}$, respectively. The first two bands in Figure 2a exhibit a vertical K profile typical of bottom-topography enhanced mixing, in which K is larger in the deeper ocean and decays upward within the water column. Indeed, the $8^\circ\text{--}10^\circ\text{N}$ and $22^\circ\text{--}24^\circ\text{N}$ bands override the Ngulu Atoll and the Kyushu-Palau Ridge and the “rough” regional bottom topography can be confirmed by the red curve in Figure 2a (bottom), showing the RMS topographic height variance in a $32\text{ km} \times 32\text{ km}$ square based on *Smith and Sandwell* [1997].

[9] In contrast to these two topographically-enhanced mixing bands, the high diffusivity band at $25^\circ\text{--}29^\circ\text{N}$ has a largely vertically-uniform K value at $\sim 2.5 \times 10^{-5}\text{ m}^2\text{ s}^{-1}$. No rough bottom topography is present below this band. Given its location just south of the semidiurnal critical latitude, it is reasonable to regard the elevated diapycnal diffusivity inferred in this band as resulting from parametric subharmonic instability. Additional evidence supporting this

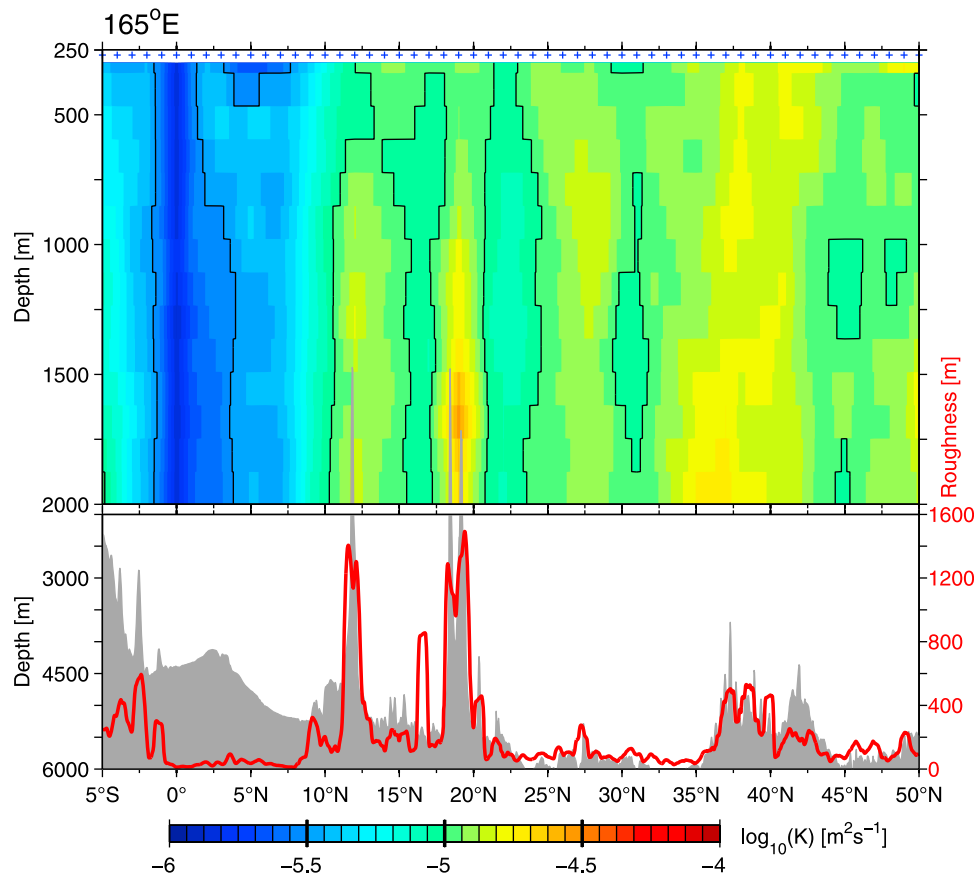


Figure 3. Same as Figure 2a except for along the 165°E repeat section. See Figure 1 for the geographical location of this section.

conjecture will be provided in the next section when the time-varying K signals from this band are analyzed.

[10] The 4th high diffusivity band along 137°E is located north of 32°N over the steep continental slope off Japan. In addition to the possibility of impinging barotropic tides interacting with the continental slope, this band is occupied by the intense western boundary current, the Kuroshio, that flows eastward and has a deep sloping permanent thermocline [e.g., Qiu and Joyce, 1992]. In Figure 2a, the highest K value next to the continental slope exceeds $5 \times 10^{-5} \text{ m}^2 \text{ s}^{-1}$. Enhanced diapycnal mixing within the band of the Kuroshio has also been found by Kunze *et al.* [2006] in their analyses of WOCE P2 and P10 CTD/ADCP data and, more recently, by Jing and Wu [2010] who analyzed a subset of the 137°E CTD data with the use of both the fine-scale parameterization and Thorpe-scale methods. While not pursued here, future studies are desired to clarify the relevant mixing processes associated with the interaction of barotropic tides, steep continental slope, and the deep Kuroshio jet.

[11] The ASUKA line is located to the immediate west of the 137°E meridian (Figure 1). This line is beneficial to our analysis as it provides an independent CTD data set to ascertain the consistency of the inferred diapycnal diffusivity. Figure 2b shows the latitude-depth section of K profiles averaged over the 38 available CTD surveys along the ASUKA line. Like along 137°E, locally enhanced diffusivity values appear over the entire 300–2,000 m water column in the 25°–29°N band and the column-averaged K has the same

$2.5 \times 10^{-5} \text{ m}^2 \text{ s}^{-1}$ value as that along 137°E. Located inside the same Shikoku Basin, the bottom topography below the 25°–29°N band along the ASUKA line is similarly devoid of roughness.

[12] The latitude-depth section for the inferred diffusivity along the 165°E meridian is shown in Figure 3. Extremely low K values of $\sim 0.2 \times 10^{-5} \text{ m}^2 \text{ s}^{-1}$ are found within the 3°-equatorial band. In agreement with the 137°E results, elevated diapycnal diffusivity is detected in bands underlain with rough bottom topography: the 11°–13°N band above the Ratak Ridge, the 18°–21°N band above the Marcus-Necker Ridge, and the 35°–42°N band above the Shatsky Rise. Within the 25°–29°N band of our interest, the inferred diffusivity is locally higher than its neighboring northern and southern regions. Averaged from 300 to 2,000 m inside the 25°–29°N band (to be denoted symbolically hereafter as $\langle \rangle$), the inferred $\langle K \rangle$ is $1.2 \times 10^{-5} \text{ m}^2 \text{ s}^{-1}$ and this value is about half of those estimated along the 137°E and ASUKA lines.

[13] As the intensity of PSI is governed by the energy transfer from low-mode semi-diurnal internal tides, the reason for this difference in $\langle K \rangle$ can be sought in the differing strength of semidiurnal internal tides along the 165°E versus 137°E/ASUKA lines. While the 25°–29°N band along 165°E is remote from major topographic features, the 25°–29°N band along 137°E is close to the Izu-Ogasawara Ridge and the Ryukyu Island Chain, the two major sites for tide-topography interaction in the northwestern Pacific Ocean (see Figure 1) [Niwa and Hibiya, 2001; Simmons *et al.*,

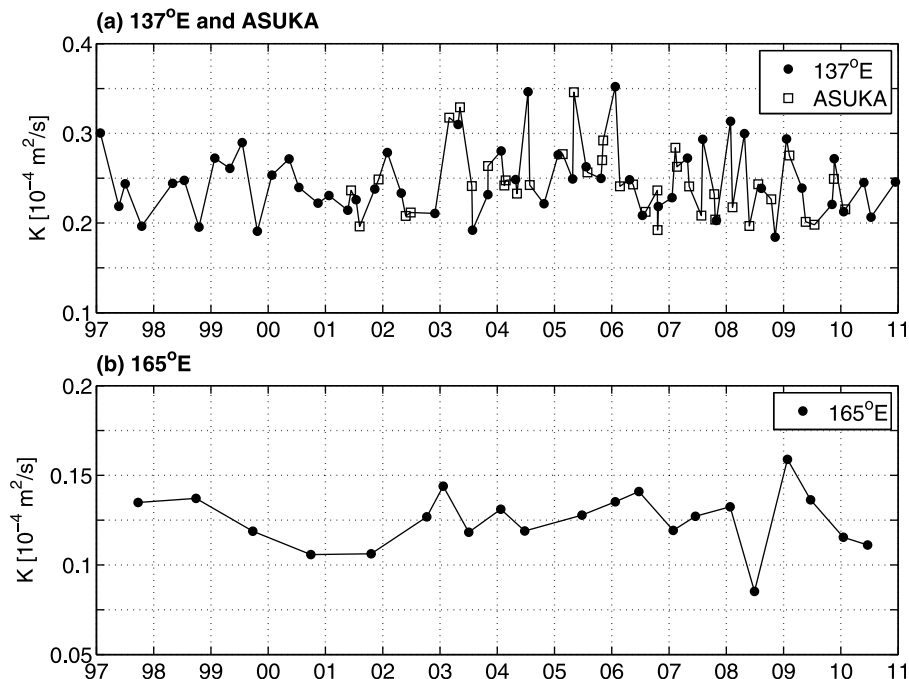


Figure 4. (a) Time series of the diapycnal diffusivity $\langle K \rangle$ averaged in the 25° – 29° N band from 300 to 2,000 m. Solid circles denote the estimates from the 137° E surveys and open squares, the estimates from the ASUKA-line surveys. (b) Same as Figure 4a except for the estimates from the 165° E surveys.

2004]. According to the recent global numerical simulation study by *Niwa and Hibiya* [2011], the depth-integrated kinetic energy for the $M_2 + S_2$ internal tide in the 25° – 29° N band along 137° E ($\sim 1,000 \text{ J m}^{-2}$) is an order of magnitude greater than that along 165° E ($\sim 100 \text{ J m}^{-2}$).

4. Time-Varying Diapycnal Eddy Diffusivity

[14] To examine the *time-varying* diffusivity signals in the 25° – 29° N band, we first construct the time series of $\langle K \rangle$ evaluated from individual CTD surveys (Figure 4). Because of their proximity, the time series inferred from the 137° E and ASUKA surveys are plotted together in Figure 4a. The fact that these two data sets can be smoothly merged into a single time series as shown in Figure 4a lends confidence to the consistency of the diffusivity values derived from the different surveys. As we noted in section 3, the time-mean $\langle K \rangle$ value along 137° E/ASUKA is about twice as large as that along 165° E (Figure 4b). At both sites, the temporal variability in $\langle K \rangle$ is large: the maximum value of $3.6 \times 10^{-5} \text{ m}^2 \text{ s}^{-1}$ in Figure 4a doubles the minimum value of $1.8 \times 10^{-5} \text{ m}^2 \text{ s}^{-1}$. Along 165° E, the detected maximum and minimum $\langle K \rangle$ values also differ by a factor of 2.

[15] To explore further the vertical structures of time-varying diffusivity signals, we conduct an empirical orthogonal function (EOF) analysis on the $K(z, t)$ values averaged within the 25° – 29° N band. Figure 5 shows the first EOF mode result from the combined 137° E and ASUKA data. This mode accounts for 36.0% of the total variance and its vertical structure exhibits a pattern corresponding roughly to the first dynamic normal mode profile calculated from the local mean potential density data (cf. Figures 5a and 5b). While no zero-crossing exists in vertical, the mode amplitude

is much reduced below the 1,500 m depth. Notice that it makes physical sense that the PSI-induced eddy diffusivity signals should have a first-mode vertical profile because PSI itself draws energy from the horizontal velocity of the internal tide that has a first-mode vertical profile [*Young et al.*, 2008]. As shown in Figure 5c, the temporal weighting function of this EOF mode is highly correlated to the $\langle K \rangle$ time series presented in Figure 4a. In other words, the dominant K variability in the 25° – 29° N band along 137° E/ASUKA has a vertical low-mode structure and its temporal changes can be effectively represented by the $\langle K \rangle$ time series.

[16] This EOF result for 137° E/ASUKA is also valid for the $K(z, t)$ data along 165° E. As shown in Figure 6, the first EOF mode along 165° E accounts for 40.8% of the total variance and its vertical structure has a zero-crossing at 1,750 m, slightly deeper than the zero-crossing depth at 1,450 m of the local first dynamic normal mode. In comparison to the vertical structure along 137° E/ASUKA, the first EOF mode along 165° E has an amplitude that weakens at a deeper depth. This difference is likely due to the fact that the first dynamic normal mode at 165° E has a deeper zero-crossing structure than that at 137° E (cf. Figures 5b and 6b). Consistent with the 137° E/ASUKA result, the temporal weighting function of the first EOF mode along 165° E is again well represented by its corresponding $\langle K \rangle$ time series.

[17] Given the relevance of the time-varying $\langle K \rangle$ signals, we examine below how they are related to the external forcing of semidiurnal tides and surface wind stresses.

4.1. Semidiurnal Tide Forcing

[18] As the energy source for PSI in the 25° – 29° N band resides ultimately in the barotropic semi-diurnal tidal current, it is of interest to clarify the connection between the

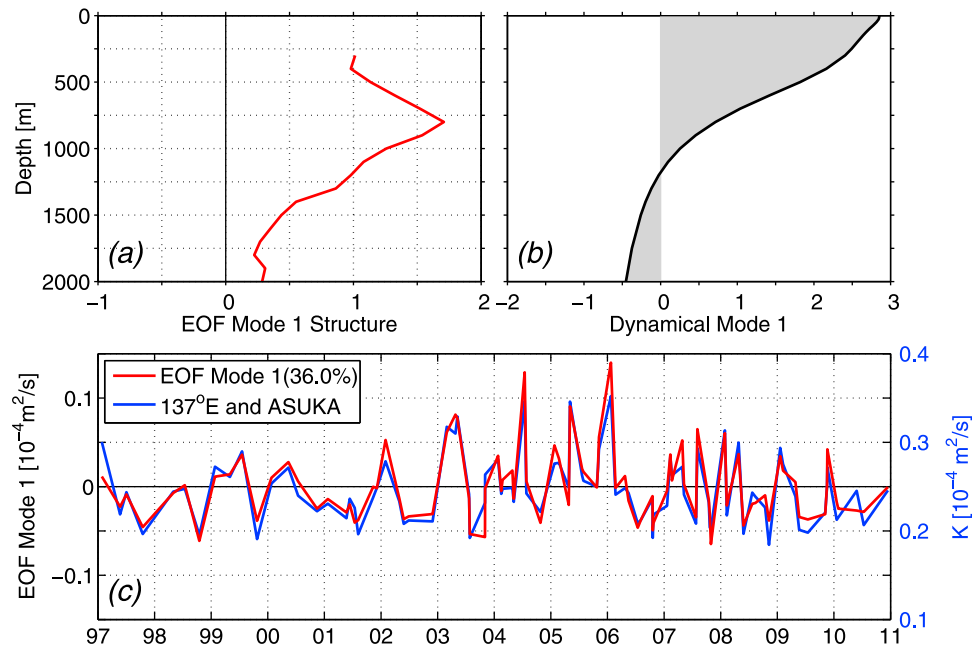


Figure 5. (a) Vertical structure of the first EOF mode for the diapycnal diffusivity $K(z, t)$ signals in 25° – 29° N from the 137° E/ASUKA CTD surveys. (b) Vertical profile of the first dynamic normal mode based on the mean potential density data at 29° N and 137° E. (c) Red line is temporal weighting function of the first EOF mode. Blue line is sectionally-averaged $\langle K \rangle$ time series (same as that shown in Figure 4a).

time-varying $\langle K \rangle$ signals and the intensity of the regional semidiurnal tides. To do so, we extract the M_2 and S_2 tidal current information from the output of the TPX07.2 global ocean tidal model developed by *Egbert et al.* [1994] and *Egbert and Erofeeva* [2002]. The model determines the complex amplitudes of M_2 , S_2 , and other tidal constituents by least-square fitting the TOPEX/Poseidon and Jason-1 and -2 along-track sea surface height data to the Laplace tidal

equations. Figure 7a shows the $M_2 + S_2$ tidal current amplitudes for January–February, 1997, at (28.9° N, 137° E) and (28.9° N, 165° E) after removal of signals with periods shorter than 2 days. At both sites, the semidiurnal tidal currents exhibit clearly-defined spring-neap cycles. Although the time-mean amplitude of the tidal current is much greater at 137° E than at 165° E (1.4 cm s^{-1} versus 0.9 cm s^{-1}), it is

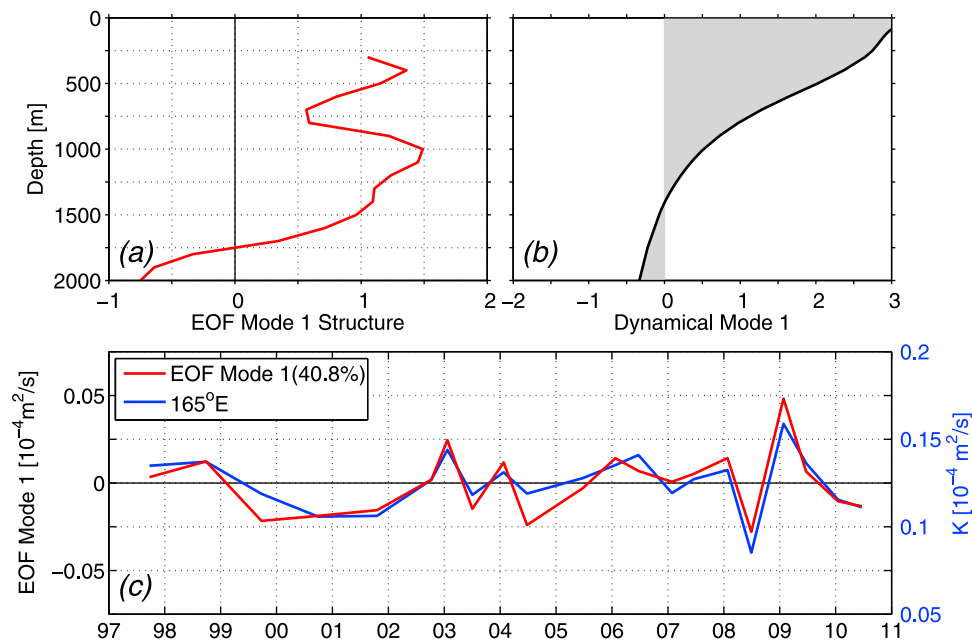


Figure 6. Same as Figure 5 except for the results along 165° E. The blue line in Figure 6c is same as that shown in Figure 4b.

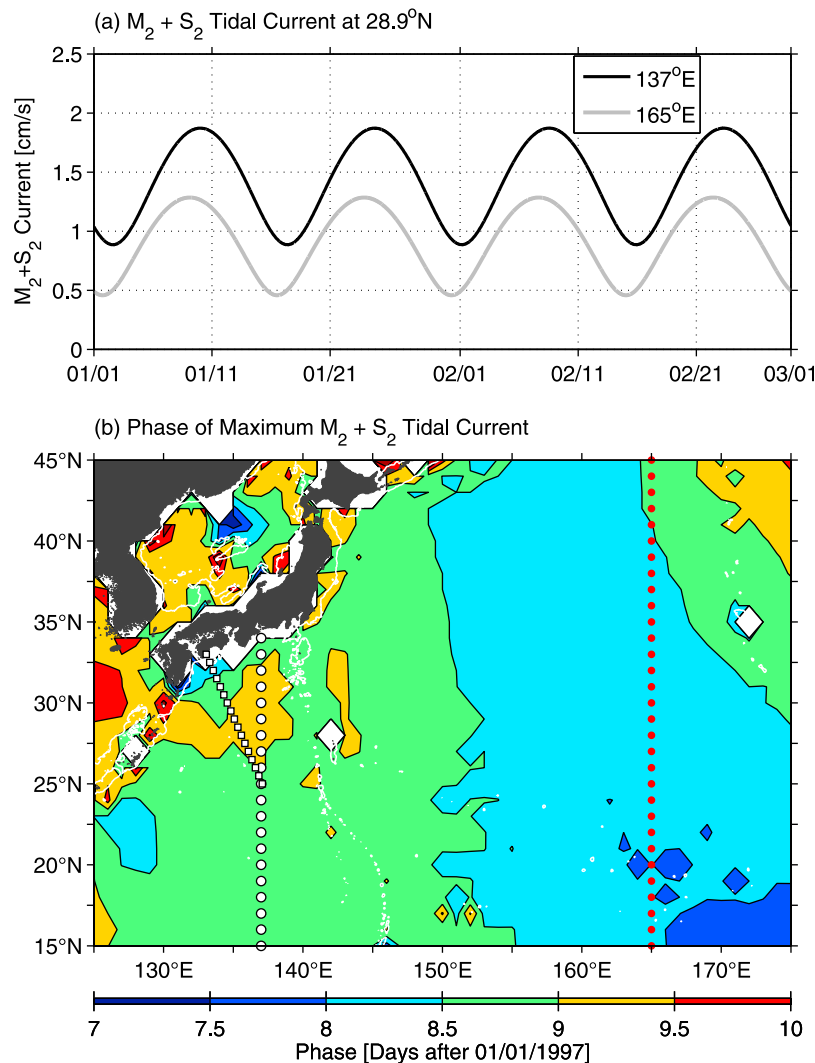


Figure 7. (a) $M_2 + S_2$ tidal current amplitudes for January–February, 1997, at 28.9°N and 137°E (black line) versus 28.9°N and 165°E (grey line). (b) Phases of maximum $M_2 + S_2$ tidal current relative to January 1, 1997. White contours indicate the 1000 m isobaths, and symbols are the same as those in Figure 1 for the locations of CTD stations. Both figures are based on the TPXO7.2 global ocean tidal model output [Egbert and Erofeeva, 2002].

interesting to note that the difference in current amplitude between the spring and neap phases is about 1 cm s^{-1} at both sites. Notice that in the western North Pacific basin between 137°E and 165°E, the M_2 and S_2 tidal current phase varies less than 1 day spatially (see Figure 7b).

[19] To quantify how this spring-neap tidal current modulation affects the $\langle K \rangle$ time series, we examine the following relationship through least-square fitting:

$$\langle K \rangle(t) = \alpha T(t - \gamma) + b(t), \quad (3)$$

where t is the date midway between when the CTD casts from 29°N to 25°N were taken during each survey, γ is the time lag of $\langle K \rangle(t)$ behind the spring-neap modulated tidal current $T(t)$, α is the regression coefficient, and $b(t)$ denotes the temporal residual. For both the 137°E/ASUKA and 165°E surveys, it takes between 1 to 3 days to complete the

nominally 1°-spacing CTD surveys between 25°N and 29°N. This time interval justifies the use of the low-pass filtered $T(t)$ time series of Figure 7a in equation (3). Physically, γ represents the time required both by the spring-neap modulated tidal currents at the critical latitude to result in turbulent mixing through the PSI mechanism and by the internal tides to propagate here from their generation sites. Figure 8a (left) shows the regression coefficient α as a function of γ for the $\langle K \rangle$ time series from 137°E/ASUKA. The maximum correlation, $\alpha = 0.24 \times 10^{-5} \text{ m}^2 \text{ s}^{-1}$ per cm s^{-1} , is found when the spring-neap modulated tidal current leads $\langle K \rangle$ by 6 days. With the local spring-neap semidiurnal tide modulating at 1 cm s^{-1} (see Figure 7a), this result indicates that $\langle K \rangle$ can differ by $0.24 \times 10^{-5} \text{ m}^2 \text{ s}^{-1}$, or 16% of the time-varying $\langle K \rangle$ signals (at the $1.5 \times 10^{-5} \text{ m}^2 \text{ s}^{-1}$ level as shown in Figure 4a), between the spring and neap phases.

[20] The scatterplot of $\langle K \rangle$ versus T time series with $\gamma = 6$ days is shown in Figure 8a (right) and the black line denotes

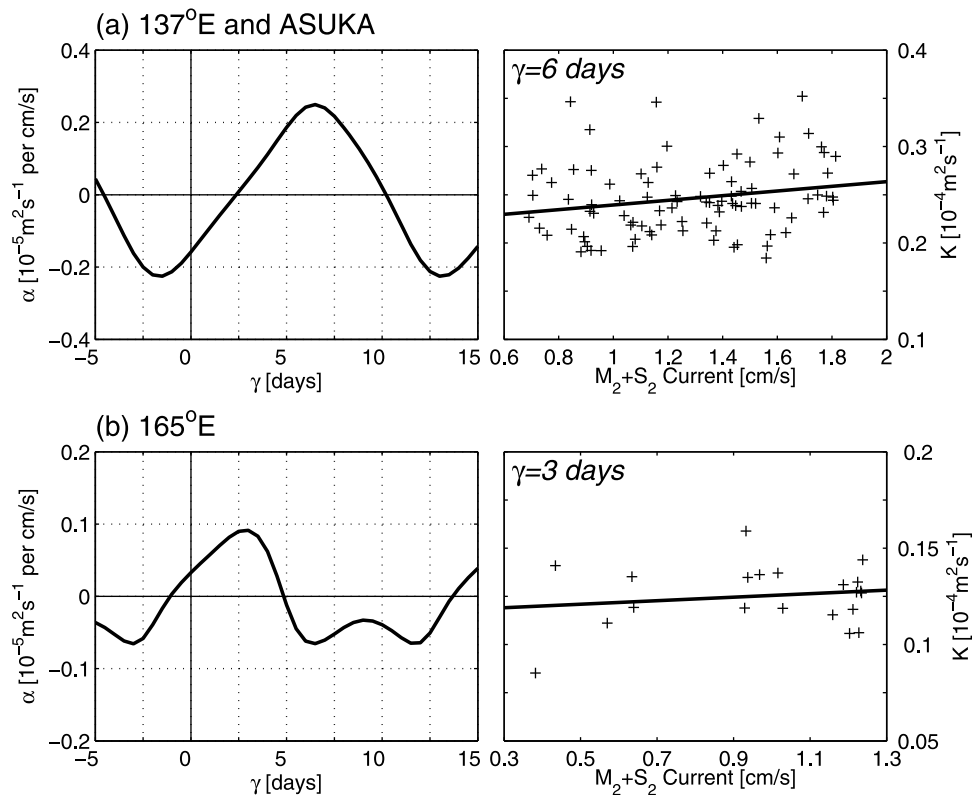


Figure 8. (a, left) Regression coefficient α as a function of time lag γ between the $\langle K \rangle$ time series and the $M_2 + S_2$ tidal current amplitude at the 137°E/ASUKA site. (a, right) Scatterplot of $\langle K \rangle$ versus the $M_2 + S_2$ tidal current amplitude at $\gamma = 6$ days. The best-fit α value is denoted by the straight line. (b) Same as Figure 8a except for the regression results at the 165°E site.

the best-fit $\alpha = 0.24 \times 10^{-5} \text{ m}^2 \text{ s}^{-1} \text{ per cm s}^{-1}$. Is this α value statistically significant? To test this, we generate 1000 time series of $\langle K \rangle$ by randomizing the order of the original 91 data points from 137°E/ASUKA (Figure 5a) and calculate the α values by fixing $T(t - \gamma)$ in equation (3). The 95% highest α value from these 1000 trials is $0.21 \times 10^{-5} \text{ m}^2 \text{ s}^{-1} \text{ per cm s}^{-1}$, indicating that the α value at $\gamma = 6$ days in Figure 8a is statistically significant above the 95% confidence level.

[21] Following the same procedures, we plot in Figure 8b the α value as a function of γ for the $\langle K \rangle$ time series from 165°E. The maximum α value is obtained when $\langle K \rangle$ lags the local spring-neap modulated tidal current by 3 days. Compared to the α value along 137°E/ASUKA, the maximum α along 165°E is smaller, $\sim 0.1 \times 10^{-5} \text{ m}^2 \text{ s}^{-1} \text{ per cm s}^{-1}$. Because the independent $\langle K \rangle$ estimates are limited to the 21 CTD surveys along 165°E, this α value is statistically significant only at the 75% confidence level. This result for 165°E, while implying a linkage between the spring-neap cycle of semidiurnal tides and the turbulent mixing in the 25°–29°N band, needs to be confirmed by future longer observations.

4.2. Surface Wind Forcing

[22] By generating near-inertial currents within the surface mixed layer, forcing by surface winds can contribute to the deeper ocean turbulent mixing after the wind-forced, near inertial waves penetrate downward [e.g., Nagasawa et al.,

2000; Alford, 2003]. Along the 137°E between 30°N and 33°N, a recent study by Jing and Wu [2010] has identified seasonal changes in the upper ocean diapycnal diffusivity that are attributable to the seasonal surface wind stress modulation. As the surface wind fluctuations in the northwestern Pacific Ocean are dominated by synoptic-scale atmospheric disturbances [e.g., Qiu et al., 2004], it is important to clarify the degree to which the inferred $\langle K \rangle$ time series depends on the energy input by the synoptic-scale surface wind forcing.

[23] To do so, we adopt the lagged regression approach similar to equation (3)

$$\langle K \rangle(t) = \beta W(t - \tau) + b(t), \quad (4)$$

where $W(t - \tau)$ denotes the wind work on near-inertial motions averaged over τ days before the date of the CTD casts in the 25°–29°N band, and β is the regression coefficient. To evaluate the wind work on near-inertial motions, we adopt the formula given by D'Asaro [1985]

$$W(t) = -Re \left[\rho \frac{Z_I}{(r - if)H} \frac{dT^*}{dt} \right], \quad (5)$$

where ρ is the density of seawater, r is the damping coefficient for the near-inertial motions ($=0.25f$ [see Watanabe and Hibiya, 2002]), H is the mixed layer depth, Z_I is the wind-induced inertial current within the mixed layer,

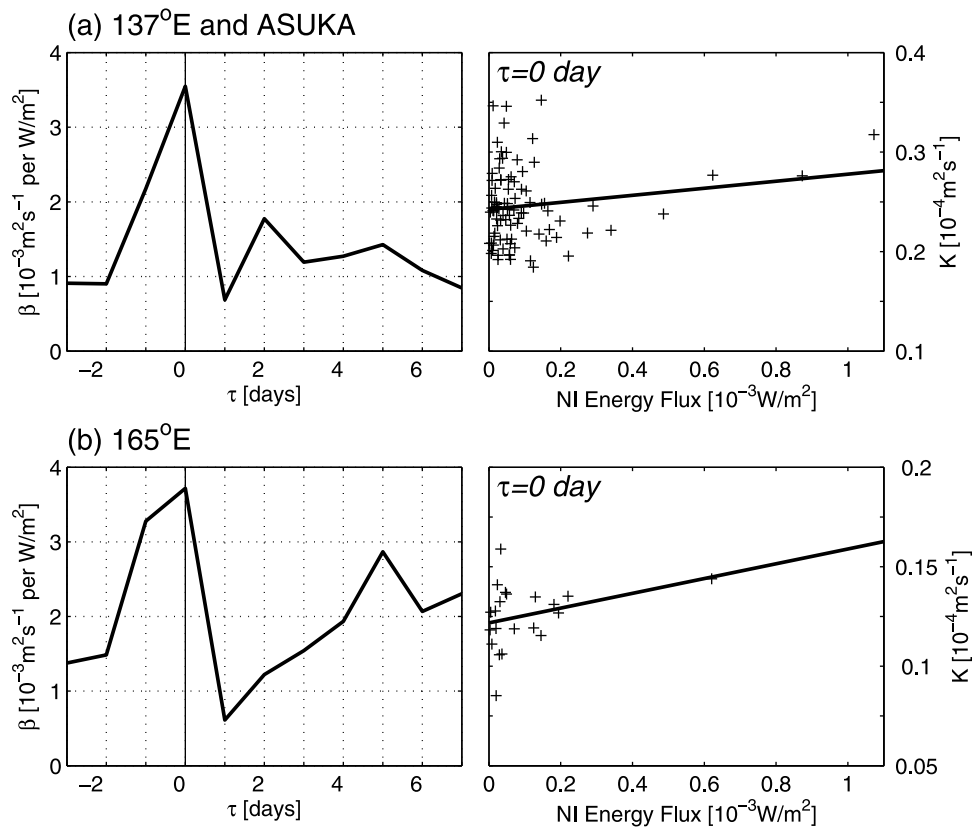


Figure 9. (a, left) Regression coefficient β as a function of time lag τ between the $\langle K \rangle$ time series and the near-inertial energy flux at the 137°E/ASUKA site. (a, right) Scatterplot of $\langle K \rangle$ versus the near-inertial energy flux at $\tau = 0$ day. The best-fit β value is denoted by the straight line. (b) Same as Figure 9a except for the regression results at the 165°E site.

$T = (\tau^x + i\tau^y)/\rho$ is the complex wind stress, and T^* is the complex conjugate of T . In equation (5), Z_I is the wind-induced inertial current in the mixed layer and is the solution to

$$\frac{dZ_I}{dt} = -(r + if)Z_I - \frac{1}{r + if} \frac{d}{dt} \left(\frac{T}{H} \right). \quad (6)$$

To evaluate $W(t)$, we solve equations (5) and (6) with the wind stress data $T(t)$ given by the 6-hourly National Centers of Environmental Prediction (NCEP) reanalysis product [Kistler *et al.*, 2001] and H by the cruise-averaged mixed layer depth within the 25°–29°N band (a minimum depth is set at 50 m). Along the 137°E/ASUKA section, the mixed layer depth H has a well-defined annual cycle with a maximum of 100–150 m in winter and a minimum of ~ 50 m in summer.

[24] Figure 9a (left) shows the regression coefficient β as a function of τ for the 137°E/ASUKA time series. The maximum β ($=3.5 \times 10^{-3} \text{ m}^2 \text{ s}^{-1} \text{ per W m}^{-2}$) is obtained when $\tau = 0$ day. This β value is significant above the 91% confidence level based on the same statistical test method described in section 4.1. With the wind work on near-inertial motions fluctuating over the range of $1.0 \times 10^{-3} \text{ W m}^{-2}$ (see Figure 9a, right), this β value indicates that the wind work-induced $\langle K \rangle$ changes have a range of $0.35 \times 10^{-5} \text{ m}^2 \text{ s}^{-1}$, or $\sim 23\%$ of the time-varying $\langle K \rangle$ value in the 25°–29°N band

along 137°E/ASUKA. This level of $\langle K \rangle$ changes is about 50% larger than that due to the fortnightly spring-neap tidal current discussed in section 4.1.

[25] Figure 9b shows the corresponding result for the 165°E site. Like at 137°E/ASUKA, the maximum regression is obtained again when the concurrent surface wind forcing is used in equation (4). The maximum β value at 165°E is $3.7 \times 10^{-3} \text{ m}^2 \text{ s}^{-1} \text{ per W m}^{-2}$, which is on a par with that at 137°E/ASUKA. Due to the limited data points used in constructing Figure 9b, this β value is statistically significant only at the 87% confidence level. As for the result presented in Figure 8b, it would be important for future studies to verify the result of Figure 9b with additional CTD surveys.

[26] Because the temporal variation of the spring-neap tidal forcing is independent of that of the wind work, it is possible to combine equations (3) and (4) into the following multiple regression model:

$$\langle K \rangle(t) = \alpha T(t - \gamma) + \beta W(t - \tau) + b(t). \quad (7)$$

Applying this model to the 137°E/ASUKA $\langle K \rangle$ time series reveals that while there are no changes for $\gamma = 6$ days and $\tau = 0$, the regression coefficient for the tidal forcing α increases from $0.24 \times 10^{-5} \text{ m}^2 \text{ s}^{-1} \text{ per cm s}^{-1}$ in equation (3) to $0.28 \times 10^{-5} \text{ m}^2 \text{ s}^{-1} \text{ per cm s}^{-1}$ and that for the wind work β , from $3.5 \times 10^{-3} \text{ m}^2 \text{ s}^{-1} \text{ per W m}^{-2}$ in equation (4) to $4.4 \times 10^{-3} \text{ m}^2 \text{ s}^{-1} \text{ per W m}^{-2}$. In other words, this combined

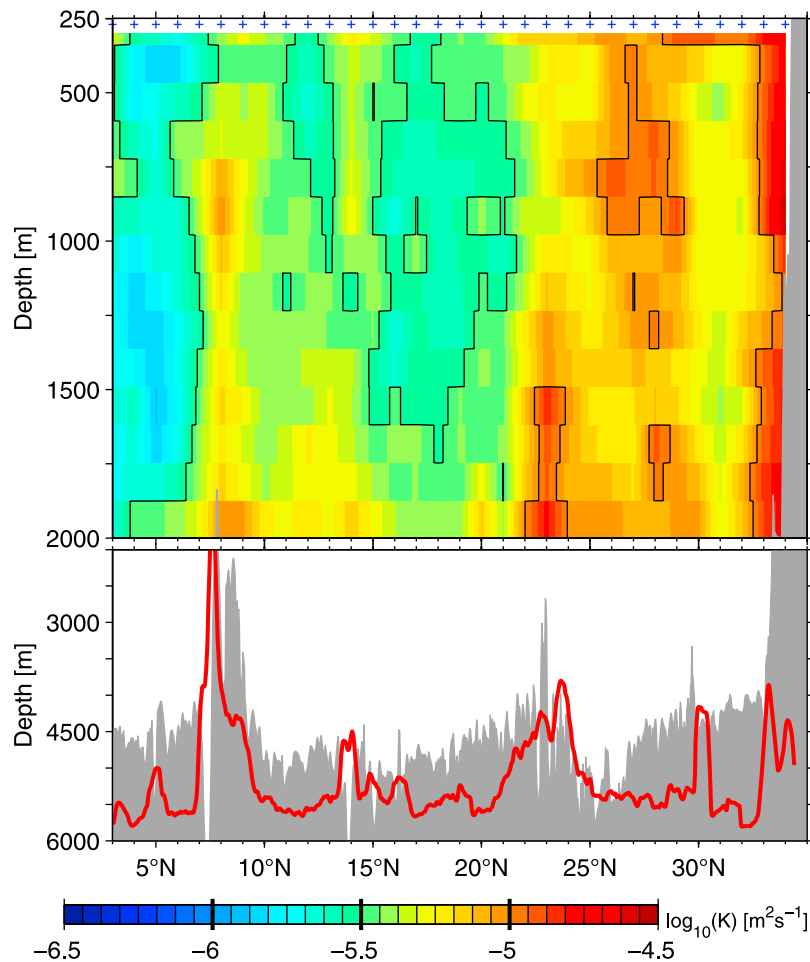


Figure 10. (top) Latitude-depth section of the standard deviation of the diapycnal diffusivity $K(y, z, t)$ inferred from 57 repeat CTD surveys along the 137°E meridian. (bottom) Same as in Figure 2a, bottom.

forcing model explains 47% of the time-varying $\langle K \rangle$ signals, as compared to the $\sim 39\%$ value based on the tidal and wind forcings separately.

[27] It is worth stressing that a constant shear/strain variance rate $R_w = 7$ has been used in this study to estimate the diapycnal diffusivity. As the near-inertial waves have much shear but little strain according to the internal wave polarization relations, this ratio is likely higher when the wind work and PSI induced near-inertial motions become stronger [Kunze *et al.*, 2006]. In other words, the amplitude of the $\langle K \rangle$ modulation by the wind work and PSI forcing is probably under-estimated with the use of a fixed R_w value in equation (1).

[28] In concluding this section, we plot in Figure 10 the standard deviation values as a function of latitude and depth for the time-varying K signals based on the 57 repeat cruises along 137°E . It is interesting to note that this y - z distribution has a spatial pattern very similar to that of the time-mean diffusivity distribution shown in Figure 2a. In other words, in all places where the time-mean K values are elevated due to either the rough topography [i.e., 7° – 10°N , 22° – 25°N], PSI [25° – 29°N] or the fluctuating Kuroshio jet [32° – 34°N], the inferred eddy diffusivity signals are also more temporally variable. The ratio of the standard deviation over the time-mean diffusivity averaged across the 137°E section is 0.33.

It will be important for future studies to explore the time-dependent K signals in the latitude bands outside of 25° – 29°N .

5. Summary

[29] We have in this study estimated the diapycnal diffusivity from the high-resolution CTD data along the JMA 137°E , 165°E , and ASUKA repeat lines in the northwestern Pacific Ocean. The estimation uses the strain variance information in the 300–2,000 m water column and follows the fine-scale parameterization formulation put forth by Kunze *et al.* [2006]. Along all the three repeat lines, enhanced vertical mixing is found at locations where major topographic features are present. At these locations, the inferred diapycnal diffusivity $K(z)$ has a bottom-enhanced vertical profile that decays with the increasing height above the bottom.

[30] Locally-elevated diapycnal diffusivity is also *consistently* detected within the 25° – 29°N band of the three repeat lines. Unlike the topography-induced $K(z)$ profile, the observed diffusivity in this band exhibits a nearly uniform vertical profile within the 300–2,000 m layer. Being just equatorward of the semi-diurnal critical latitude and devoid of rough regional bottom topography, this high diapycnal diffusivity band of 25° – 29°N is indicative of the enhanced

turbulent mixing resulting from parametric subharmonic instability. Longitudinally, the time-mean $\langle K \rangle$ value averaged in the 300–2,000 m layer of 25°–29°N at the western 137°E and ASUKA sites is twice as large as that at the 165°E site (2.5×10^{-5} versus $1.2 \times 10^{-5} \text{ m}^2 \text{ s}^{-1}$). This spatial difference in $\langle K \rangle$ is due to the proximity of the 137°E and ASUKA sites to the two major internal semidiurnal tide generation hot spots in the northwestern Pacific Ocean: the Izu-Ogasawara Ridge and the Ryukyu Island Chain [Niwa and Hibiya, 2001; Simmons et al., 2004].

[31] Along both 137°E/ASUKA and 165°E, an EOF analysis of the time-varying diffusivity signals in the 25°–29°N band revealed that the vertical structure of their respective dominant modes bears a resemblance to the vertical profile of the local first dynamic normal mode. Specifically, the time-varying $K(z, t)$ signals are vertically coherent above the 1,500–1,700 m depth and their amplitudes tend to diminish below that depth. In practice, this allowed us to examine the time-varying diffusivity signals in the 300–2,000 m water column by focusing on the $\langle K \rangle$ time series.

[32] To examine the time-varying $\langle K \rangle$ signals, we first quantified their connection to the magnitude of the local, barotropic, semidiurnal tidal currents. Based on a lagged regression analysis, we found that there exists a correlation (significant above the 95% confidence level) when the spring-neap modulated $M_2 + S_2$ tidal current leads the $\langle K \rangle$ time series by 6 days at the 137°E/ASUKA site. With the regression coefficient $\alpha = 0.24 \times 10^{-5} \text{ m}^2 \text{ s}^{-1} \text{ per cm s}^{-1}$, the tidal current induced diffusivity variations can reach 10% the time-mean $\langle K \rangle$ level (of $2.5 \times 10^{-5} \text{ m}^2 \text{ s}^{-1}$) and 16% of the time-varying $\langle K \rangle$ level (of $1.5 \times 10^{-5} \text{ m}^2 \text{ s}^{-1}$), respectively. At the 165°E site, a similar connection between the spring-neap modulated $M_2 + S_2$ tidal current and the inferred $\langle K \rangle$ was derived. The regression coefficient estimated at this site, however, lacked statistical significance due to the small number of the available CTD surveys.

[33] In addition to the tidal current forcing, we have also evaluated the impact of the regional surface wind forcing upon the time-varying $\langle K \rangle$ signals. For the 137°E/ASUKA site, we again found a statistically significant correlation between the $\langle K \rangle$ time series and the concurrent wind work signals on near-inertial motions. With the regression coefficient estimated at $\beta = 3.5 \times 10^{-3} \text{ m}^2 \text{ s}^{-1} \text{ per W m}^{-2}$, the wind work-induced $\langle K \rangle$ changes have a range of $0.35 \times 10^{-5} \text{ m}^2 \text{ s}^{-1}$. Though low in statistical significance, a qualitatively similar connection was also found between the concurrent surface wind forcing and the $\langle K \rangle$ time series at the 165°E site. Finally, the explained time-varying $\langle K \rangle$ signal at the 137°E/ASUKA site is increased from ~39% to 47% when the forcing of spring-neap tide and wind work is considered jointly through a lagged multiple regression model.

[34] There exist several factors that can contribute to the unaccounted-for $\langle K \rangle$ variance by the tidal and wind forcings. Measurement errors inherent in the CTD casts can introduce random and systematic errors in the inferred strain signals used in equation (1). The fine-scale parameterization method itself, as we noted in the section concerning the ratio R_w , is subject to uncertainties. With regard to the external forcings, we have neglected in this study the potential impact of mesoscale eddies [see Jing et al., 2011]. The 25°–29°N band in the western North Pacific Ocean is frequented by

mesoscale eddies detached from the unstable Kuroshio/Kuroshio Extension jet [Ebuchi and Hanawa, 2000; Qiu and Chen, 2005]. The influence relating to the intensity and polarity of mesoscale eddies need to be quantified in future studies.

[35] Along the semidiurnal critical latitude away from the 137°E/ASUKA site, another hot spot for PSI-enhanced turbulent mixing in the North Pacific Ocean is between the dateline and 155°W [Simmons, 2008] (see Figure 3). This hot spot is located to the north of the Hawaiian Ridge and has been the focus of several recent observational and modeling studies [MacKinnon and Winters, 2005; Alford et al., 2007; Zhao et al., 2010; Hazewinkel and Winters, 2011]. For this northern Hawaii site, the semidiurnal internal tides are generated south of the critical latitude and a relevant research topic has been how the northward-propagating, ridge-induced, internal tides modify/dissipate nonlinearly as they approach the 28.9°N critical latitude.

[36] Unlike the northern Hawaii site, the 137°E/ASUKA site is located between the Izu-Ogasawara Ridge and the Ryukyu Island Chain. Both of these two topographic features are roughly meridionally aligned and are responsible for generating the regional semidiurnal internal tides. The topography-induced semidiurnal internal tides in this case would propagate zonally, rather than meridionally as in the northern Hawaii case. It would be interesting for future studies to clarify how the PSI processes and the resultant turbulent mixing are affected by the zonally-propagating semidiurnal internal tides and contrast the results to those from the northern Hawaii case.

[37] **Acknowledgments.** We thank the three anonymous reviewers whose detailed comments helped improve an early version of the manuscript. The repeat hydrographic data were provided by Japan Meteorological Agency and the surface wind stress data by National Centers of Environmental Prediction (NCEP). This research was supported by ONR (N00014-10-1-0267) and by NSF (OCE-0926594).

References

- Alford, M. H. (2003), Improved global maps and 54-year history of wind-work on ocean inertial motions, *Geophys. Res. Lett.*, *30*(8), 1424, doi:10.1029/2002GL016614.
- Alford, M. H., J. A. MacKinnon, Z. Zhao, R. Pinkel, J. Klymak, and T. Peacock (2007), Internal waves across the Pacific, *Geophys. Res. Lett.*, *34*, L24601, doi:10.1029/2007GL031566.
- Carter, G. S., and M. C. Gregg (2006), Persistent near-diurnal internal waves observed above a site of M_2 barotropic-to-baroclinic conversion, *J. Phys. Oceanogr.*, *36*, 1136–1147.
- D'Asaro, E. (1985), The energy flux from the wind to near-inertial motions in the mixed layer, *J. Phys. Oceanogr.*, *15*, 943–959.
- Ebuchi, N., and K. Hanawa (2000), Mesoscale eddies observed by TOLEX-ADCP and TOPEX/POSEIDON altimeter in the Kuroshio recirculation region south of Japan, *J. Oceanogr.*, *56*, 43–57.
- Egbert, G. D., and S. Y. Erofeeva (2002), Efficient inverse modeling of barotropic ocean tides, *J. Atmos. Oceanic Technol.*, *19*, 183–204.
- Egbert, G. D., A. F. Bennett, and M. G. G. Foreman (1994), TOPEX/Poseidon tides estimated using a global inverse model, *J. Geophys. Res.*, *99*, 24,821–24,852.
- Gregg, M. C., and E. Kunze (1991), Internal wave shear and strain in Santa Monica basin, *J. Geophys. Res.*, *96*, 16,709–16,719.
- Gregg, M. C., T. B. Sanford, and D. P. Winkel (2003), Reduced mixing from the breaking of internal waves in equatorial ocean waters, *Nature*, *422*, 513–515.
- Hazewinkel, J., and K. B. Winters (2011), PSI of the internal tide on a β plane: Flux divergence and near-inertial wave propagation, *J. Phys. Oceanogr.*, *41*, 1673–1682.
- Hibiya, T., and M. Nagasawa (2004), Latitudinal dependence of diapycnal diffusivity in the thermocline estimated using a finescale parameterization, *Geophys. Res. Lett.*, *31*, L01301, doi:10.1029/2003GL017998.

- Imawaki, S., et al. (2001), Satellite altimeter monitoring the Kuroshio transport south of Japan, *Geophys. Res. Lett.*, *28*, 17–20.
- Jing, Z., and L. Wu (2010), Seasonal variation of turbulent diapycnal mixing in the northwestern Pacific stirred by wind stress, *Geophys. Res. Lett.*, *37*, L23604, doi:10.1029/2010GL045418.
- Jing, Z., L. Wu, L. Li, C. Liu, X. Liang, Z. Chen, D. Hu, and Q. Liu (2011), Turbulent diapycnal mixing in the subtropical northwestern Pacific: Spatial-seasonal variations and role of eddies, *J. Geophys. Res.*, *116*, C10028, doi:10.1029/2011JC007142.
- Kistler, R., et al. (2001), The NCEP-NCAR 50-year reanalysis: Monthly means CD-ROM and documentation, *Bull. Am. Meteorol. Soc.*, *82*, 247–267.
- Kunze, E., E. Firing, J. M. Hummon, T. K. Chereskin, and A. M. Thurnherr (2006), Global abyssal mixing inferred from lowered ADCP shear and CTD strain profiles, *J. Phys. Oceanogr.*, *36*, 1553–1576.
- MacKinnon, J. A., and K. B. Winters (2005), Subtropical catastrophe: Significant loss of low-mode tidal energy at 28.9°, *Geophys. Res. Lett.*, *32*, L15605, doi:10.1029/2005GL023376.
- McComas, C., and F. Bretherton (1977), Resonant interaction of oceanic internal waves, *J. Geophys. Res.*, *82*, 1397–1412.
- Muller, P., G. Holloway, F. Henyey, and N. Pomphrey (1986), Nonlinear interactions among internal gravity waves, *Rev. Geophys.*, *24*, 493–536.
- Nagasawa, M., Y. Niwa, and T. Hibiya (2000), Spatial and temporal distribution of the wind-induced internal wave energy available for deep water mixing in the North Pacific, *J. Geophys. Res.*, *105*, 13,933–13,943.
- Nagasawa, M., T. Hibiya, Y. Niwa, W. Watanabe, Y. Isobe, S. Takagi, and Y. Kamei (2002), Distribution of fine-scale shear in the deep waters of the North Pacific obtained using expandable current profilers, *J. Geophys. Res.*, *107*(C12), 3221, doi:10.1029/2002JC001376.
- Niwa, Y., and T. Hibiya (2001), Numerical study of the spatial distribution of the M_2 internal tide in the Pacific Ocean, *J. Geophys. Res.*, *106*, 22,441–22,449.
- Niwa, Y., and T. Hibiya (2011), Estimation of baroclinic tide energy available for deep ocean mixing based on three-dimensional global numerical simulations, *J. Oceanogr.*, *67*, 493–502.
- Qiu, B., and S. Chen (2005), Variability of the Kuroshio Extension jet, recirculation gyre and mesoscale eddies on decadal timescales, *J. Phys. Oceanogr.*, *35*, 2090–2103.
- Qiu, B., and T. M. Joyce (1992), Interannual variability in the mid- and low-latitude western North Pacific, *J. Phys. Oceanogr.*, *22*, 1062–1079.
- Qiu, B., S. Chen, and P. Hacker (2004), Synoptic-scale air-sea flux forcing in the western North Pacific: Observations and their impact on SST and the mixed layer, *J. Phys. Oceanogr.*, *34*, 2148–2159.
- Rainville, L., and R. Pinkel (2006), Propagation of low-mode internal waves through the ocean, *J. Phys. Oceanogr.*, *36*, 1220–1236.
- Simmons, H. L. (2008), Spectral modification and geographic redistribution of the semi-diurnal internal tide, *Ocean Modell.*, *21*, 126–138.
- Simmons, H. L., R. W. Hallberg, and B. K. Arbic (2004), Internal wave generation in a global baroclinic tide model, *Deep Sea Res., Part II*, *51*, 3043–3068.
- Smith, W. H. F., and D. T. Sandwell (1997), Global seafloor topography from satellite altimetry and ship depth soundings, *Science*, *277*, 1956–1962.
- Tian, J., L. Zhou, and X. Zhang (2006), Latitudinal distribution of mixing rate caused by the M_2 internal tide, *J. Phys. Oceanogr.*, *36*, 35–42.
- Watanabe, M., and T. Hibiya (2002), Global estimates of the wind-induced energy flux to inertial motions in the surface mixed layer, *Geophys. Res. Lett.*, *29*(8), 1239, doi:10.1029/2001GL014422.
- Young, W. R., Y.-K. Tsang, and N. J. Balmforth (2008), Near-inertial parametric subharmonic instability, *J. Fluid Mech.*, *607*, 25–49.
- Zhao, Z., M. H. Alford, J. A. MacKinnon, and R. Pinkel (2010), Long-range propagation of the semidiurnal internal tide from the Hawaiian Ridge, *J. Phys. Oceanogr.*, *40*, 713–736.